

PAPER

Cite this: *J. Mater. Chem. C*,
2024, 12, 8105Transition metal-doped SrTiO₃: when does a
tiny chemical impact have such a great
structural response?†Mikhail V. Talanov,^{id}*^a Adam I. Stash,^{id}^b Sergey A. Ivanov,^c Elena S. Zhukova,^{id}^a
Boris. P. Gorshunov,^a Boris M. Nekrasov,^{id}^a Alexander V. Melentev,^a
Vladislav I. Kozlov,^{id}^{de} Valery M. Cherepanov,^f Sergey Yu. Gavrilkin,^g
Aleksey Yu. Tsvetkov,^g Ilya A. Zavidovskiy,^h Mikhail K. Tatmyshevskiy,^h
Maxim Savinov,ⁱ Valery M. Talanov^j and Alexander A. Bush^d

The effect of doping on the chemical and physical properties of semiconductors, alloys, ferroelectrics, glasses, and other substances has been a classic topic in materials science for centuries. Strontium titanate, SrTiO₃, is an archetypal perovskite of interest for both fundamental science as quantum paraelectric and numerous outstanding physical properties and applications, including dielectrics, tunable microwave and photovoltaic devices, superconductors, thermoelectrics, potential multiferroics. Its chemical doping with transition metals leads to new functionalities, but intrinsic mechanisms of structural responses, activated by impurities, have not been systematically investigated. Herein, we present the results of a comparative study of the crystal structure, vibrational spectra, and dielectric properties of SrTiO₃:M (M = Mn, Ni, and Fe, 2 at%) single crystals. It is shown that impurities constitute a different tendency to off-centering and the formation of dipoles: Mn and Fe atoms are shifted from the center of the oxygen octahedron, while Ni atoms remain on-centered. As a result, small chemical doping has a dramatic effect on the dielectric response through various structural mechanisms, including the pseudo Jahn–Teller effect, the first-order Jahn–Teller effect, and defect-induced distortion. These findings open up fundamentally new possibilities for the practical solution of a difficult problem: controlling the dielectric responses of quantum paraelectrics by choosing the type of chemical additive.

Received 13th January 2024,
Accepted 14th May 2024

DOI: 10.1039/d4tc00180j

rsc.li/materials-c

^a Laboratory of Terahertz Spectroscopy, Center for Photonics and 2D Materials, Moscow Institute of Physics and Technology, 9 Institutskiy Pereulok, Dolgoprudny, Moscow Region 141700, Russia. E-mail: mvtalanov@gmail.com^b A. N. Nesmeyanov Institute of Organoelement Compounds of Russian Academy of Science, 28 Vavilov st., Moscow 119991, Russia^c Chemical Department, Moscow State University, 1 Leninskie Gory, Moscow 119991, Russia^d Research Institute of Solid-State Electronics Materials, MIREA – Russian Technological University (RTU MIREA), 78 Vernadsky prospect, Moscow 119454, Russia^e Kapitza Institute for Physical Problems RAS, 2 st. Kosygina, Moscow 119334, Russia^f National Research Center “Kurchatov Institute”, 1 ac. I.V. Kurchatov square, Moscow 123182, Russia^g P. N. Lebedev Physical Institute of the Russian Academy of Sciences, Moscow 119991, Russia^h Center for Photonics and 2D Materials, Moscow Institute of Physics and Technology, 9 Institutskiy Pereulok, Dolgoprudny, Moscow Region 141700, Russiaⁱ Institute of Physics, Czech Academy of Sciences, 18200 Prague 8, Czech Republic^j Platov South-Russian State Polytechnic University, 346428, Novocherkassk, Russia† Electronic supplementary information (ESI) available. See DOI: <https://doi.org/10.1039/d4tc00180j>

1. Introduction

Chemical doping is probably the most common and natural strategy for tuning the physical properties of a broad range of functional materials. The best-known example is semiconductors, whose electronic structure can be controlled by the types of impurity atoms and defects that provide the required charge carriers: electrons or holes. This approach is implemented in the form of industrially developed technologies that make it possible to create materials for electronic, optical, magnetic, luminescent, photovoltaic, photocatalysis, plasmonic, optical, thermoelectric, and many other applications.^{1–9} A similar logic is relevant for dielectrics, allowing one to achieve colossal permittivity in advanced capacitor materials (grouped into Colossal Permittivity Materials^{10–12}) such as doped and co-doped CaCu₃Ti₄O₁₂,^{10,13,14} BaTiO₃,^{15–17} TiO₂,^{10,11,18} NiO,^{10,19} and other systems.¹⁰ Predominantly extrinsic contributions, including interface effect (internal barrier layer capacitance), defect dipole, or polaron hopping, have the greatest impact on

the dielectric response of these materials.^{10,12} For dilute systems, the intrinsic lattice dielectric response, as well as its composition-induced change, is often neglected, and dopants act rather as a source of charge-compensated defects and related defect-induced local distortions.

Ferroelectrics and related materials with highly polarizable crystal lattices and pronounced structure–property relationships deviate from this general trend. In this regard, chemical substitution can lead to the appearance of quenched random electric fields and local strains, driving the system toward a glassy or relaxor state with enhanced dielectric and electromechanical properties.^{20–25} For example, in the case of $\text{PbMg}_{1/3}\text{Nb}_{2/3}\text{O}_3\text{–PbTiO}_3$ solid solution, the aliovalent substitution of only 2.5 mol% Pb^{2+} on Sm^{3+} leads to a sharp increase (almost twice) in the piezoelectric response d_{33} to record values for both single crystals and ceramics: up to 4100 pC/N²⁶ and 1500 pC/N,²⁷ respectively. In the case of the most common in modern technology piezoelectric $\text{PbZr}_{1-x}\text{Ti}_x\text{O}_3$ system, the type of dopant determines the ferroelectric hardness or softness of the macroscopic responses of the ceramics. Doping with donor ions, such as La^{3+} for the A-position or Nb^{5+} for the B-position, leads to the formation of A-cation vacancies, while doping with acceptor ions, such as Na^+ for the A-position or Mn^{3+} for the B-position, contributes to the emergence of oxygen vacancies in ABX_3 perovskites.²⁸ The former type of defect enhances the mobility of domain walls, which results in ferroelectrically soft properties; the latter acts as a pinning centre for domain walls motion, causing ferroelectrically hard behaviour.^{29,30} However, the response of ferroelectrics consists of both extrinsic and intrinsic contributions, the ratios between which differ in various compounds, and their establishment is a matter of debate.³⁰ Therefore, the question is still relevant and pressing: what intrinsic mechanisms, activated by the entry of small amounts of impurities, are involved in the formation of structural responses?

In this context, the study of weakly doped (no more than a few at%) quantum paraelectric SrTiO_3 (STO) takes on new colours despite more than half a century of research history. First, let us note the uniqueness of single crystals of quantum paraelectrics: the dielectric properties are determined exclusively by the contribution of the dynamics of the ferroelectric soft mode (SM), which softens upon cooling, but remains stable up to subhelium temperatures, and a phase transition does not occur. This means that the dielectric dispersion is negligible and that the intrinsic contributions play a dominant role, which makes single crystals of quantum paraelectrics an ideal object for studying the structural mechanisms activated by the impurities.^{25,31} Second, the rich STO phase diagrams constructed in different coordinates, as well as proximity of the compound to the quantum critical point,^{32,33} make it possible to induce the ferroelectric state in various ways: by misfit strain in thin films,³⁴ application of uniaxial pressure,³⁵ strong DC,³⁶ or terahertz-pulse electric fields.³⁷ Moreover, the ferroelectric state can be achieved through the substitution of cations^{38–41} and anions (oxygen isotope exchange),⁴² as well as through defect engineering.⁴³ Third, chemical doping of STO with

transition metal atoms can lead to the emergence of new physical phenomena and functionality, including glassy/relaxor properties,⁴⁴ multiferroic properties,⁴⁵ superconductivity,⁴⁶ and critical quantum multiferroicity.⁴⁷ Fourth, STO containing transition metals has already found chemical applications as mixed electronic-ion conductor materials,^{48,49} catalysts,⁵⁰ oxygen storage,⁵¹ and anodes in fuel cells,⁵² highlighting the need for a thorough comprehension of the associated mechanisms of structure formation.

Thus, the main goal of this work is to establish the mechanisms of the structure and dielectric properties' formation in weakly doped STO:M (M = Mn, Ni, and Fe, 2 at%) single crystals. For the first time, we carried out precision single-crystal X-ray diffraction experiments and discovered different tendencies towards local off-centring of impurity atoms within oxygen octahedron (Section 2). Moreover, signatures of the structural distortion mechanisms were found through a comprehensive study of terahertz-infrared (THz-IR) and Raman spectra (Section 3), as well as the temperature dependences of the low-frequency dielectric permittivity. We show that the small ionic entry into the STO structure leads to drastic changes in dielectric behaviour, controlled by the type of dopant (Section 4). We associate the origins of the observed differences in structural response, activated by weak chemical doping, with the manifestation of the Jahn–Teller and the pseudo Jahn–Teller effects, which we discuss within the framework of vibronic coupling theory (Section 5).

2. Single crystal X-ray diffraction

Fig. 1 shows the reciprocal space projections (Fig. 1a–c) and corresponding maps of residual electron density distribution (Fig. 1d–i) obtained for single crystals STO:M (M = Mn, Ni, and Fe, 2 at%) (Fig. S1, ESI†) at room temperature (293 K). We have not found any traces of impurity phases, including transition metal oxides, which contribute to the apparent “spin glass” behaviour of the magnetic susceptibility.⁵³ Moreover, for any of the samples, no anomalies indicating the presence of phase transitions were found in the temperature dependence of the magnetic susceptibility (Fig. S2, ESI†). All the crystals under study have a cubic structure with $Pm\bar{3}m$ space group. The chemical doping of STO with $a = 3.90410(6)$ Å by transition metals leads to a slight increase in the lattice parameter, with the highest changes ($\sim 0.14\%$) being observed for Ni- and Fe-doped crystals (Table 1). Refinement of the occupancies of the cationic positions in the doped single crystals confirms the M \rightarrow Ti substitution within only the B-sublattice of the perovskite structure, while the A-sublattice occupied by strontium remains strictly stoichiometric within a standard deviation (Table S1, ESI†).

The substitution of titanium for manganese leads to the formation of residual electron density maxima shifted relative to the centre of the octahedron (Fig. 1d).⁵⁴ Precision structure refinement (GOF = 1.193) according to the model with disordered off-centred displacement of Mn cations showed that

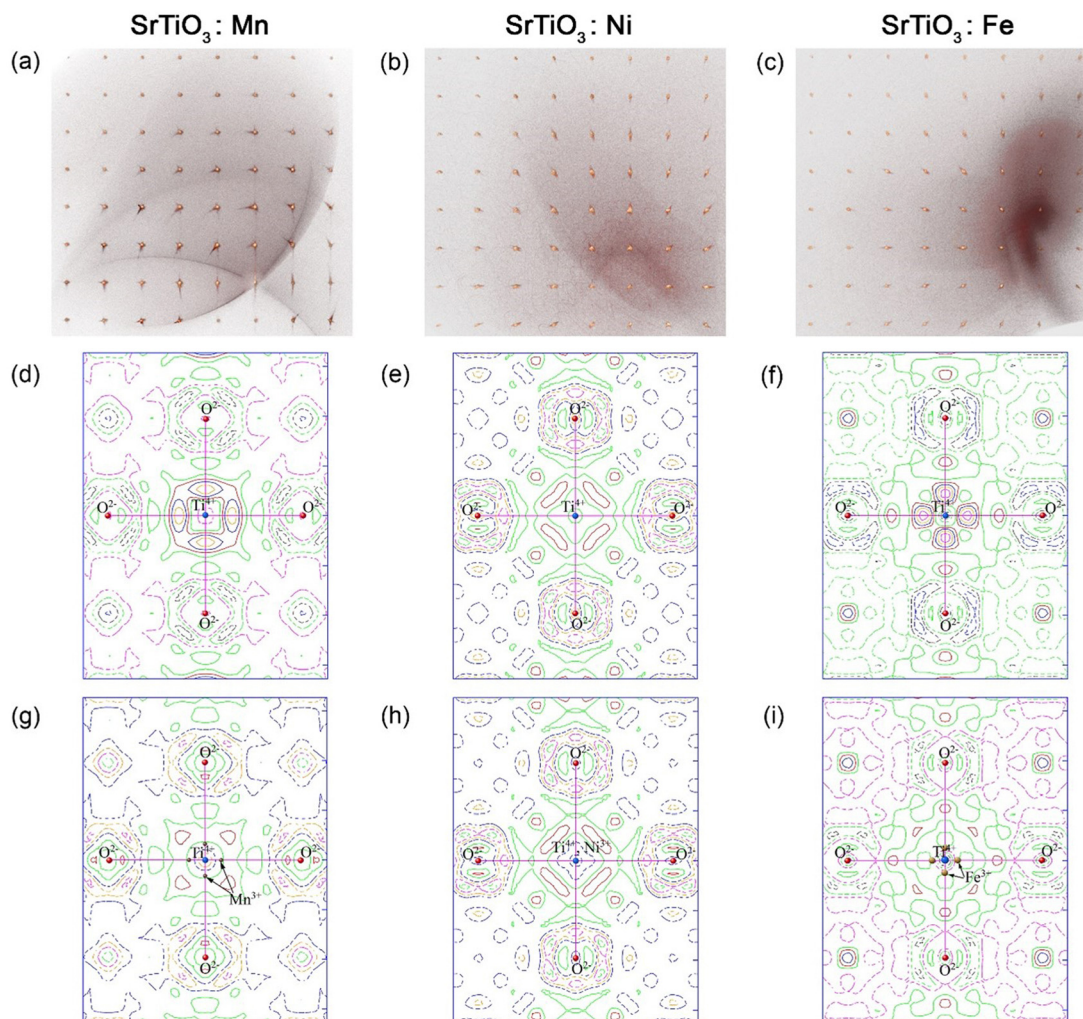


Fig. 1 (a)–(c) Reciprocal space diffraction peaks obtained by pixel-by-pixel conversion of 1200 experimental frames, measured for STO:M ($M = \text{Mn}$, Ni and Fe , 2 at%) single crystals at 293 K. (d)–(i). Maps of residual electron density distribution of single crystals STO:Mn (d) and (g), STO:Ni (e) and (h) and STO:Fe (f) and (i) without (d)–(f) and with (g)–(i) M cations at special positions (off-centred for Mn and Fe, and on-centred for Ni). Clearly visible in panels d and f is the presence of residual electron density outside the centre of the octahedron, which indicates an off-centred position of Mn and Fe atoms, while there are no such signs for Ni atoms. Negative isolines are marked with dotted lines, positive ones with solid lines. Isolines step is $0.1 \text{ e } \text{Å}^{-3}$.

the Mn Wyckoff position $6f$ is shifted by $0.33(10) \text{ Å}$ from the $1b$ Wyckoff position occupied by Ti cations. The absence of the residual electron density maxima for the structural model with off-centred positions of Mn indicates the validity (correctness) of this finding (Fig. 1g). The occupancy of the Mn off-centred position is approximately 3%, while the occupancy of the anion $3c$ Wyckoff position is 99.0%, which reflects a slight oxygen deficiency (Table S1, ESI[†]).

Substitution by Ni atoms demonstrates the opposite tendency, *i.e.*, there are no clear residual electron density maxima outside the central position in the model without accounting for Ni atoms (Fig. 1e). Putting Ni in the centre of the octahedron does not lead to noticeable changes in the electron density distribution, which confirms the on-centred position for Ni cations (Fig. 1h). This conclusion is consistent with the results of the EXAFS study made by Sluchinskaya *et al.*,⁵⁵ who found that in solid-state synthesized $\text{SrTi}_{1-x}\text{Ni}_x\text{O}_3$ powder, nickel

occupied an on-centred position, and its charge state is close to 4^+ . In contrast to this, Ni^{3+} or Ni^{2+} charge states are suggested based on the results of EXAFS and EPR for hydrothermally synthesized samples⁵⁶ and single crystals.^{57,58} Note that any charge state except 4^+ requires the formation of charge compensation vacancies, for example $\text{Ni}^{3+} - \text{V}_\text{O}$, leading to significant octahedral distortion with the Ni^{3+} displacement away from V_O by $\sim 0.33 \text{ Å}$.⁵⁸ This value is comparable to the Mn off-centring clearly observed by our single crystal diffraction (Fig. 1d and g), however, we did not observe any sign of the displaced position for Ni as well as oxygen deficiency in the studied single crystal.

Compared to the above, substitution by Fe in STO single crystals results in an intermediate position of Fe, between Mn with a clear off-centred position and Ni without any sign of the displaced position. On the one hand, there are maxima of residual electron density shifted by $\sim 0.25(5) \text{ Å}$ from the centre

Table 1 Parameters of the X-ray diffraction experiment and the final results of crystal structure refinements for the M (M = Fe, Ni, Mn)-doped and pure SrTiO₃ single crystals at room temperature

Compounds	Sr(Ti _{0.98} Fe _{0.02})O ₃	Sr(Ti _{0.98} Ni _{0.02})O ₃	Sr(Ti _{0.98} Mn _{0.02})O ₃	SrTiO ₃
Crystal data				
Molecular mass	183.64	183.70	183.38	183.48
Crystal system, space group, No Z	Cubic, <i>Pm</i> $\bar{3}$ <i>m</i> , 221			
<i>a</i> (Å)	3.90957(3)	3.90961(3)	3.90663(3)	3.90410(6)
<i>V</i> (Å ³)	59.757(1)	59.759(1)	59.622(1)	59.506(3)
Crystal size (mm)	0.059 × 0.053 × 0.041	0.127 × 0.114 × 0.067	0.121 × 0.094 × 0.083	0.114 × 0.080 × 0.066
Radiation type, wavelength	Mo-K α , λ = 0.71073 Å			
Absorption correction μ (mm ⁻¹)	25.325	25.453	25.48	25.47
Data collection				
Diffractometer	Bruker APEX II with PHOTON-II detector			
Range θ for data collection (°)	5.21–49.52			
Absorption correction	Numerical (SADABS2016/2; Bruker, 2019)			
<i>T</i> _{min} , <i>T</i> _{max}	0.379, 0.594	0.167, 0.496	0.211–0.442	0.192–0.409
No. of measured, independent and observed [<i>I</i> > 2 σ (<i>I</i>)] reflections	3552, 91, 88	4340, 91, 90	3640, 82, 80	2665, 74, 74
<i>R</i> _{int}	0.023	0.025	0.0199	0.0196
Structure refinement				
<i>R</i> [<i>F</i> ² > 2 σ (<i>F</i> ²)], <i>wR</i> (<i>F</i> ²), GOF	0.0110, 0.0224, 1.250	0.0100, 0.0235, 1.199	0.0097, 0.0231, 1.193	0.0092, 0.0230, 1.245
No. of reflections	91	91	82	74
No. of parameters	10	8	10	6
$\Delta\rho_{\max}/\Delta\rho_{\min}$ (e Å ⁻³)	0.434/–0.423	0.345/–0.448	0.358/–0.341	0.338/–0.420
Extinction coefficient	0.196(17)	0.26(2)	0.103(16)	0.090(15)

(Fig. 1f). However, placing Fe cations in the maxima worsens the quality of structural refinement (thermal oscillation parameters become negative), while accounting for Fe in the central position leaves the residual electron density maxima practically unchanged. Therefore, we used thermal parameters equal to those of the Ti cation and refined the structure with manual selection of the weight scheme. As a result, the electron density peak disappeared, indicating an off-centre position of Fe (Fig. 1i). However, we cannot confidently state (as in the case of STO:Mn) whether the Fe impurity is displaced from the centre or not within the accuracy of the experimental procedure, which requires additional evidence to complement the existing results. The ambiguous picture of Fe-displacement in the STO:Fe crystal follows a pronounced tendency to mix Fe³⁺/Fe⁴⁺ valence coexistence in SrTi_{1-x}Fe_xO₃ solid solutions, where the valence ratio depends on *x*⁵⁹ and different structural mechanisms are involved in local distortion around Fe³⁺ (compensated oxygen vacancies increasing with *x* growth⁶⁰) and Fe⁴⁺ (Jahn–Teller effect weakening as *x* increases⁶¹).

3. Vibrational spectroscopy

We used complementary Raman and THz-IR spectroscopy techniques to reveal a more detailed picture of lattice dynamics in the crystals with different metal dopants. The vibrational representation (*G*_{vibr}) of a cubic perovskite contains three IR-active *F*_{1u} phonons and one silent *F*_{2u} vibration. Thus, in the IR spectra of a cubic STO:M (M = Mn, Ni, and Fe, 2 at%) crystals, only three triply degenerate polar modes with *F*_{1u} symmetry can appear (for each mode there are transverse (TO) and

longitudinal (LO) phonons), while first-order Raman lines are symmetry forbidden.

Fig. 2 shows the combined THz-IR spectra of the reflection coefficient *R* for STO:M (M = Mn, Ni, and Fe, 2 at%) crystals measured at room temperature. Foremost, we note that all the spectra have typical features of STO crystals and are characterized by the presence of three main lines^{62–64} with frequencies: $\nu_{\text{TO}_1} = 88 \text{ cm}^{-1}$ and $\nu_{\text{LO}_1} = 175 \text{ cm}^{-1}$, $\nu_{\text{TO}_2} = 175 \text{ cm}^{-1}$ and $\nu_{\text{LO}_2} = 266 \text{ cm}^{-1}$, $\nu_{\text{TO}_4} = 545 \text{ cm}^{-1}$ and $\nu_{\text{LO}_4} = 795 \text{ cm}^{-1}$ for Slater, Last and Axe mode, respectively. Note that all spectra practically coincide at frequencies $\nu > 150 \text{ cm}^{-1}$; only in the case of STO:Ni we notice an enhanced tendency for peak splitting at $\nu \sim 275\text{--}480 \text{ cm}^{-1}$ and $\nu \sim 525\text{--}790 \text{ cm}^{-1}$. As can be seen from the Fig. 2, the difference is observed in the low-frequency region of the spectrum ($\nu < 150 \text{ cm}^{-1}$), where the soft ferroelectric mode (TO₁) of the Slater type occurs. This is especially important since the temperature dynamics of this mode almost completely determines the radio-frequency dielectric response of STO crystals due to their ultimately low dielectric dispersion in the intermediate MHz–GHz frequency range.⁶⁵ Based on the THz-IR data, we can conclude that the *R*(ν) dependence of the Ni-doped crystal is the same as in pure STO, while the behaviour of STO:Mn significantly deviates from it (Fig. 2, inset). The Fe-doped crystal occupies an intermediate position between the two extreme cases, with a small (within the experimental uncertainty) increase in *R*(ν) values relative to the *R*(ν) curve of pure STO. Here, one important remark is in order. In our reasoning, we are basing on rather small changes (or non-changes) of experimentally measured reflection coefficient. Corresponding measurements were repeated many times, in various conditions, with different pure STO and

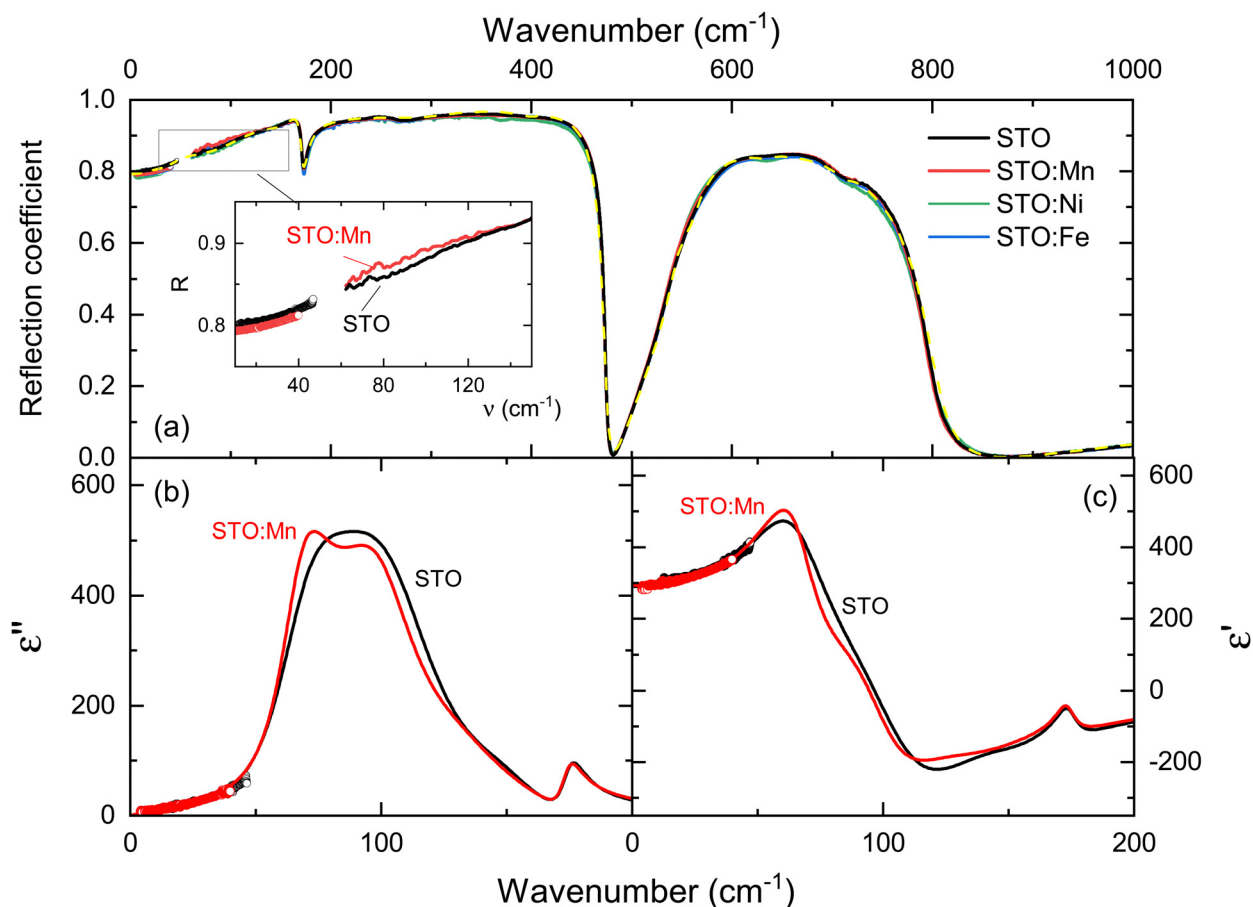


Fig. 2 (a) Terahertz-infrared spectra of reflection coefficient of STO:M (M = Mn, Ni and Fe, 2 at%) single crystals measured at room temperature. Dashed line shows typical least-square fit for the STO:Mn sample with the model of coupled Lorentzians. Dots below 40–50 cm⁻¹ indicate THz data calculated basing on the directly measured THz spectra of real and imaginary parts of dielectric permittivity, that are shown in panels (b) and (c), respectively, together with the FIR permittivity spectra (lines) corresponding to the fit presented by dashed line in panel (a).

doped STO samples. All the results we are relying on are reliable and reproducible. This separation according to the type of low-frequency part of the combined THz-IR spectra correlates with the results of the single-crystal X-ray diffraction, where Ni atoms occupy the centre of the octahedron, Mn is strongly off-centred, while displacements of Fe atoms from the octahedra centre are smaller in the amplitude and less pronounced. Since the reflection coefficient value is strongly sensitive to dielectric parameters values, the observed deviation of the $R(\nu)$ curve of the STO:Mn crystal at low frequencies indicates the significant effect of Mn-doping on the soft mode (SM) characteristics. Note, that coupling of SM with relaxation processes of the atomic hopping type is typical for many disordered systems^{66–68} and leads to a change in the phonon contribution to the dielectric permittivity, like in A-site Mn²⁺ doped STO with off-centred impurity ions.⁶⁹ We observe very similar temperature behaviour of the SM in the case of the Mn-doped single crystal under study. Moreover, the low-frequency phonon (SM for pure STO) acquires a more complex double structure with frequency splitting and intensity redistribution (Fig. 2b), which clearly indicates changes in the intrinsic (phonon) dielectric response.

Room-temperature Raman spectra of the STO:M single crystals demonstrate the presence of scattering features in four main frequency regions: 100–500 cm⁻¹, 600–800 cm⁻¹, around 1000 cm⁻¹ and around 1600 cm⁻¹ (Fig. 3 and Fig. S2–S4, ESI[†]). The spectral response is governed by the second-order scattering processes due to multiphonon interactions, and all the main features are characteristic of the well-known Raman spectra of STO single crystal.^{62,70} Therefore, below, we consider in detail the signatures inherent in the spectra of doped crystals.

The Raman spectra of the Ni-doped STO single crystal is characterized by a drastic increase in the intensity of maxima at $\nu = 665$ cm⁻¹ in comparison with other samples. Note that for crystals of the perovskite family the stretching modes, in particular the Jahn–Teller-type distortions, dominate in the high-frequency region of the spectrum.^{71–73} This type of local vibration appears in Raman spectra in many systems with electron-degenerate octahedral states, including such crystals as LaMnO₃,⁷² TbMnO₃,⁷⁴ LaCoO₃,⁷⁵ CaRuO₃,⁷⁶ and many others. The closest example for comparison is oxidized Sr(Fe_xTi_{1-x})O₃ (*i.e.*, with Fe⁴⁺ ions), demonstrating the local Jahn–Teller distortion.^{61,77} In its Raman spectra, the

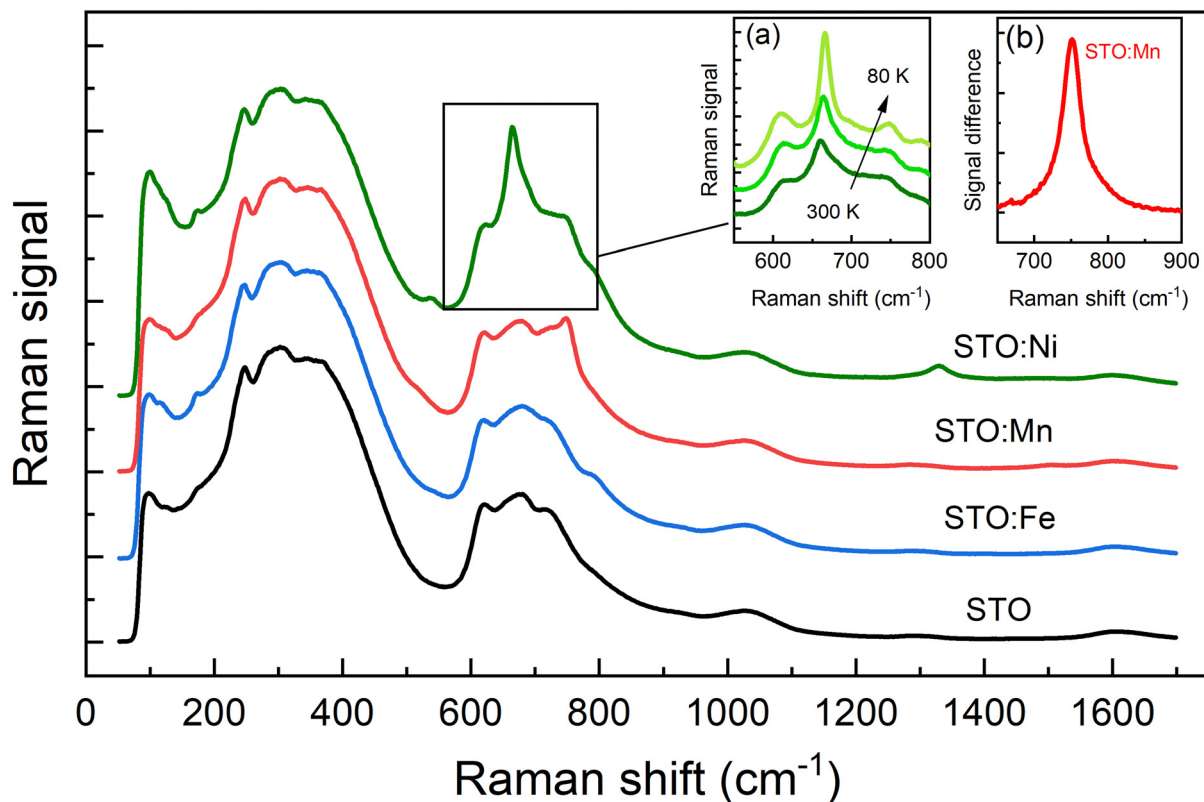


Fig. 3 Raman spectra of STO:M (M = Mn, Ni and Fe, 2 at%) crystals measured at room temperature. Inset (a) shows temperature dependent Raman spectra of Ni-doped single crystal. Inset (b) shows signal difference (obtained by subtracting the spectrum of the pure STO) for Mn-doped single crystals.

appearance and increase in intensity of the line at 690 cm^{-1} are observed with decreasing Fe concentration. This behaviour is explained by the fact that at low Fe concentrations, the delocalization of d electrons does not occur, and the Jahn–Teller effect is not suppressed. However, in reduced $\text{Sr}(\text{Fe}_x\text{Ti}_{1-x})\text{O}_{3-x/2}$ samples with coexisting Fe^{3+} and oxygen vacancies (as shown by X-ray absorption spectroscopy), this specific line is not observed.⁶¹ Moreover, the temperature behaviour of this line, which is a signature of local Jahn–Teller distortion in perovskites, in our case is in good agreement with the example considered: the intensity of the line increases significantly, and its FWHM decreases upon cooling (Fig. 3 inset a). This indicates the possible Jahn–Teller nature of local distortion in STO:Ni single crystal, *i.e.*, the presence of Ni^{3+} ions is implied. At the same time, the absence of obvious signs of an intensity increase of this vibration (compared to pure STO) indicates the absence of Jahn–Teller local distortions in STO:Mn and STO:Fe single crystals, which can exclude a significant amount of Mn^{3+} and Fe^{4+} ions.

A distinctive feature of the Raman spectra of STO:Mn single crystal is the presence of additional excitation at a frequency of 750 cm^{-1} , which we emphasized using difference analysis in comparison with a pure STO (Fig. 3, inset b). This type of vibration is also observed in the ceramics $\text{SrTi}_{1-x}\text{Mg}_x\text{O}_{3-x}$ (the line intensity increases with x) with substitution in B-site, but not in A-substituted solid solutions $\text{Sr}_{1-x}\text{Mg}_x\text{TiO}_3$.⁷⁸ As was previously shown by Zheng *et al.*,⁷⁹ the appearance of an

additional line at $750\text{--}850\text{ cm}^{-1}$ in B-substituted complex perovskites is common and is associated with a local violation of the inversion centre if, in particular, two different B cations occupy neighbouring octahedra. In the case of STO:Mn, the local symmetry breaking is caused not only by the size differences of the two types of B-cations, but also by the significant Mn atoms off-centring, detected by single crystal XRD (Fig. 1), which explains the reasons for such a strong intensity of the additional line (Fig. S2, ESI†). The spectrum of the STO:Fe single crystals is characterized by the absence of this excitation. Instead, it reveals few weak lines (Fig. S3, ESI†), which correspond to contributions of various $\text{Fe}^{3+}\text{-V}_\text{O}$ complexes with small iron displacements ($\sim 0.1\text{ \AA}$), as predicted by the quantum mechanical calculations.⁸⁰

Thus, the Mn atoms off-centring, and, to a lesser extent, Fe, discovered from the single crystal XRD, as well as the central position of Ni atoms, find their obvious manifestations in the spectral response. Such different tendencies of impurities to induce various types of local distortions in the STO structure predetermine the diversity of dielectric properties, which we discuss below.

4. Dielectric behaviour

The discovered static (X-ray diffraction) and dynamic (vibrational spectroscopy) signs of local structural distortions are a

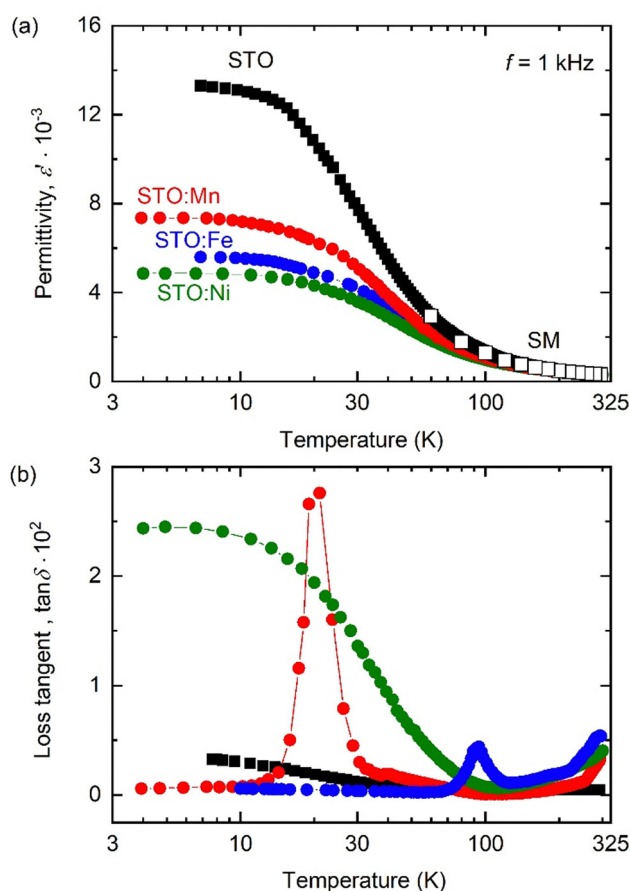


Fig. 4 Temperature dependences of dielectric permittivity (a) and $\tan \delta$ (b) of single crystals STO:M (M = Mn, Ni, and Fe, 2 at%) and pure STO measured at $f = 1$ kHz. (a) Open dots correspond to temperature-dependent dielectric strength $\Delta \varepsilon_{\text{SM}}$ of terahertz soft mode. Data for pure STO are presented for comparison, since this makes it possible to clearly recognize the effect of chemical doping and the contribution from dipoles of various types against the background of soft mode dynamics.

key prerequisite for the formation of various types of dipoles in the host of the STO crystal lattice. The dielectric contribution from the temperature-activated dipole dynamics is expected to be most pronounced against the background specified by the temperature behaviour of the STO soft mode. Fig. 4 demonstrates the comparative temperature dependences of real part of dielectric permittivity (ε') and loss tangent ($\tan \delta$) of single crystals STO:M (M = Mn, Ni, and Fe, 2 at%) and pure STO measured at a frequency (f) of 1 kHz on cooling. The temperature dependences of the real permittivity of all single crystals exhibit properties typical for pure STO,⁸¹ including SM-related dielectric behaviour at low f (*i.e.*, absence of dielectric dispersion) and a distinct step-like anomaly at temperatures below an antiferrodistortive transition (~ 105 K for pure STO), without any signs of a ferroelectric phase transition (a). Transition-metal doping leads to the suppression of the saturation ε' value from 13 000 for pure STO to 7300, 5600, and 4800 for Mn, Fe, and Ni-doped crystals, respectively. It is interesting to note that the low-temperature value of ε' is inversely proportional to the

relative atomic mass of the B-site metal (ε' decreases as STO \rightarrow STO:Mn \rightarrow STO:Fe \rightarrow STO:Ni), but this is not confirmed in the IR spectra, where such ratios are more substantiated for intrinsic (lattice) effects. Temperature dependences of dielectric losses show even more dramatic differences in the temperature behaviour for single crystals STO:M (Fig. 4b). While in the pure STO single crystal $\tan \delta(T)$ -curve undergoes a monotonic increase from $\sim 2.8 \times 10^{-4}$ at $T > 75$ K to $\sim 3.0 \times 10^{-3}$ at $T \approx 10$ K, the temperature dependences of doped crystals are fundamentally different. There is a pronounced dielectric loss peak with high intensity ($\tan \delta(T)$ increases about 50 times at the maximum compared to the background values) and low width (FWHM < 10 K) observed at ~ 20 K for the STO:Mn single crystal. Temperature behavior of dielectric loss of the STO:Fe single crystal demonstrates much less pronounced diffuse maximum in $\tan \delta(T)$ (it increases by about 20 times, FWHM ≈ 20 K) at temperatures close to antiferrodistortive phase transition. At the same time, $\tan \delta$ values of the STO:Ni single crystal increase by a factor of 30 when cooled below 100 K, reaching saturation at ~ 10 K. Unlike other crystals, the temperature behaviour of the dielectric losses of STO:Ni follows the trend of the $\varepsilon'(T)$ curve, and $\tan \delta$ values are highest at low temperatures, which indicates an incipient relaxation process (Fig. 4b). All doped crystals have a high-temperature anomaly at $T > 300$ K, which is usually associated with the relaxation of compensating oxygen vacancies. Note that this anomaly is the strongest in the STO:Fe crystal.

To reveal the features of such drastic differences in the dielectric properties of STO:M (M = Mn, Ni, and Fe, 2 at%) single crystals, we carried out a comparative analysis of the dielectric measurement results in more detail (Fig. 5). The dependences of dielectric permittivity $\varepsilon'(T)$ and dielectric contribution of the terahertz soft mode $\Delta \varepsilon_{\text{SM}}(T)$ of doped crystals are qualitatively similar to each other and to their behaviour observed in pure STO. At high temperatures, they follow the Curie–Weiss behaviour (inset in Fig. 5a, c and e): $\Delta \varepsilon_{\text{SM}}(T) = C/(T - T_C)$; where C is the Curie constant and T_C is the approximate Curie temperature. The subsequent cooling below 100 K results in a deviation of the $1/\varepsilon'(T)$ dependence from the linear Curie–Weiss law, which is attributed to quantum fluctuations and coupling with acoustic phonons.^{32,82–85} Traditionally, this quantum paraelectric behaviour is described with the Barrett expression⁸⁶ (inset in Fig. 5a, c and e):

$$\varepsilon'(T) = C / \left(\frac{T_1}{2} \coth \frac{T_1}{2T} - T_C \right),$$

where T_1 is the so-called quantum temperature below which quantum fluctuations become significant. In all doped STO crystals, the parameters of the Barrett equation are very close to each other (Fig. 5a, c, and e), as well as to those of pure STO with $T_1 = 80$ K and $T_C = 35.5$ K.⁸² The difference $T_1 - 2T_C$ characterizes the tendency of a system to ferroelectric ordering: $T_1 > 2T_C$ indicates the suppression of ferroelectric state and, consequently, the stability of quantum paraelectric state, while $T_1 < 2T_C$ is a foreshadowing for incipient ferroelectric behaviour or even a transition to a long-range ferroelectric order.

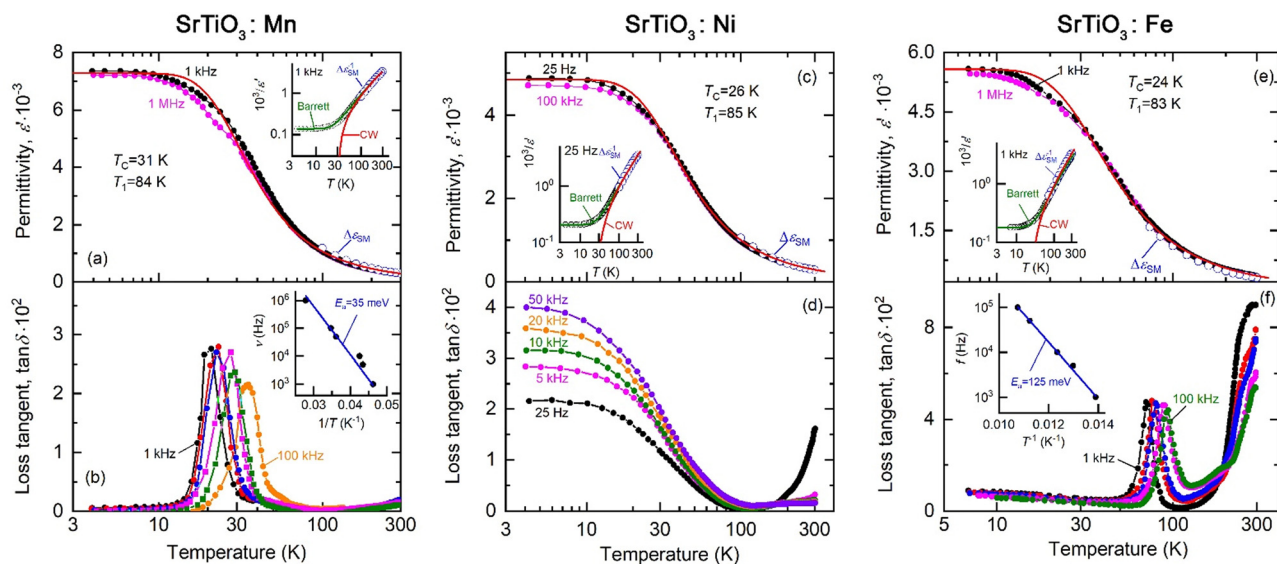


Fig. 5 Temperature dependences of dielectric parameters and soft mode parameters of single crystals STO doped by 2 at% of Mn (a) and (b),⁵⁴ Ni (c) and (d), and Fe (e) and (f), measured at different frequencies in radio-frequency and terahertz ranges. (a), (c) and (e) Temperature dependences of real dielectric permittivity ϵ' is measured at several frequencies. Open dots correspond to temperature-dependent dielectric strength of terahertz soft mode. Insets in panels (a), (c) and (e) show temperature dependences of inverse dielectric permittivity at 1 kHz (black dots) and of inverse dielectric strength of terahertz soft mode (blue dots). Solid lines show results of least-square fits with Barrett (green line) and Curie–Weiss (red line) expressions. (b), (d) and (f) Temperature dependence of loss tangent measured at several frequencies. Insets in panels (b) and (f) show Arrhenius plots of maximum frequency from temperature dependences of $\tan \delta$.

Thus, we can conclude that transitional-metal doping leads to enhancement of $T_1 - 2T_C$ that means increased stability of quantum paraelectric-type behaviour, especially for STO:Ni and Fe with $T_1 - 2T_C = 33$ K and 35 K, respectively.

As noted above, the most dramatic differences between the dielectric behaviours of crystals studied appear in the temperature dependences of dielectric losses (Fig. 4b). Fig. 5b, d and f compare the $\tan \delta$ temperature dependences of single crystals STO:M (M = Mn, Ni, Fe, 2 at%) measured at different frequencies. All doped crystals exhibit well pronounced dielectric relaxation behaviours in different temperature ranges (for $f = 1$ –100 kHz): 20–40 K and 70–95 K for STO:Mn (Fig. 5b) and STO:Fe (Fig. 5f), respectively, while the STO:Ni crystals demonstrate significant low-temperature dispersion of $\tan \delta$ without shift of maxima temperature with frequency (Fig. 5d). The absence of obvious dispersion of real part of dielectric permittivity in all samples and extremely low values of dielectric losses indicate a negligibly small role of possible extrinsic contributions, such as Maxwell–Wagner relaxation, in the dielectric relaxation at $T < 150$ K. The observed relaxation processes are described by Arrhenius law (Fig. 5b and f, Inset): $f \sim f_0 \exp(-E_a/k_B T)$ where k_B , E_a , and f_0 is the Boltzmann constant, activation energy and preexponential factor (attempt frequency), respectively. Following the Arrhenius law indicates the absence of a strong correlation between the reorientation of various dipoles contributing to the dielectric relaxation process, which is due to the low concentration of dopants diluted in the lattice.

In the case of the STO:Mn crystals, the observed two relaxation processes (main peak and diffused shoulder) have very

similar values of $E_a = 35/43$ meV and $f_0 = 1 \times 10^{10}/1.6 \times 10^{10}$ Hz (Fig. 5b). Two distinct peaks in the dielectric loss with practically the same relaxation parameters were found for STO:Mn crystals with a lower doping level of 1 at%.⁸⁷ We link the existence of this dielectric relaxation with atomic hopping between off-centred crystallographic positions, which agrees with the results of precision single crystal X-ray diffraction (Fig. 1g) and THz-IR spectroscopy (Fig. 2). Moreover, as shown earlier,⁵⁴ near the temperature of the antiferrodistortive transition, the off-centred Mn-position splits into two ones, providing the unequal potential barrier's distribution for possible local atomic hopping, which can give rise to several relaxation processes activated at low temperatures. Note that neither polishing (Fig. S5, ESI[†]) nor high-temperature annealing (Fig. S6, ESI[†]) of the single crystal significantly affect dielectric relaxation, which excludes the critical role of the surface layer and oxygen vacancies, respectively.

A fundamentally different type of relaxation process with diffused $\tan \delta$ maxima and $E_a = 125$ meV occurs in the STO:Fe crystals at temperatures close to the antiferrodistortive transition (Fig. 5f). Relatively high values of E_a and an established off-centred Fe position (Fig. 1i) indicate the defect-complex reorientation as a possible reason for the dielectric relaxation, as known for other perovskites. In particular, Nowick *et al.*⁸⁸ and Bykov *et al.*⁸⁹ reveal this type of relaxation process for Mn²⁺-doped KTaO₃ crystals, according to the results of dielectric studies at different atmospheres and EPR spectroscopy. It is also consistent with Siegel and Müller, who suggested the displacement of transition-metal ions by a distance of 0.2 Å towards the compensated oxygen vacancy V_O in Mn²⁺- and Fe³⁺-doped

SrTiO₃ crystals.⁹⁰ A similar relaxation process with $E_a \sim 120$ meV is observed in pure STO near the antiferrodistortive transition, which is usually associated with the dynamics of ferroelastic domain walls.^{91,92} The significant role of oxygen vacancies in the formation of the dielectric relaxation is indicated by its (as well as the high-temperature anomaly) significant suppression after annealing at 1400 °C (Fig. S7, ESI†).

In contrast to Fe- and Mn-doped samples with off-centred impurities, STO:Ni crystals do not exhibit any dielectric loss peaks at an accessible temperature range of 4–300 K (Fig. 5d). Instead, there is an unexpectedly strong enhancement of dielectric losses, accompanied by the appearance of significant frequency dispersion on cooling. The increase in dielectric losses with frequency and the absence of dielectric loss peaks mean that a possible relaxation process has higher values of the mean relaxation frequency (estimated as 100 kHz at 5 K). This process also differs from the low-temperature non-Arrhenius behaviour with low values of $E_a = 5.7$ meV, inherent to pure STO crystals⁹¹ and related to the polaron hopping mechanism.⁹³ For this reason, we have designated such a specific temperature-frequency behaviour as incipient relaxation, which requires further experimental study.

5. Discussion

Our experimental results demonstrate the critical effect of adding small amounts of transition metal dopants on the manifestation of local structure distortions and dielectric properties, primarily at radio frequencies. One of the main structural conditions for the occurrence of dielectric relaxation is the formation of dipoles of various types, the reorientation of which contributes to the dielectric response at the measuring frequency of the signal below the characteristic relaxation frequency of the corresponding process. Precision single crystal X-ray diffraction results reveal off-centred positions of Mn and Fe atoms, while Ni atoms occupy a position at the centre of the oxygen octahedron in the STO single crystal. Moreover, the detected clear signatures in the Raman and THz-IR spectra of specific distortions are in good agreement with the X-ray diffraction data. Thus, the key question is the reasons for the local off-centring of the doped ions and the atomic substitution scheme (related to the dipole type), which lead to the observed diversity of dielectric behaviour.

Considering the variable valence of transition metals and even the coexistence of different valence states in one sample, let's try to build arguments of local off-centring in the most general manner in terms of the vibronic coupling theory of the pseudo Jahn–Teller effect.^{94–101} We also note that adequate application of density functional theory (DFT) for dilute systems with transition metal impurities can be problematic, which also explains our inclination towards more rigorous reasoning based on symmetry principles. In addition, the experimental study of local distortions, defect configurations, and various valence states of impurity transition metals by EPR and other local structure techniques is a long-term problem

that requires separate studies (for Mn-doped STO this problem is described in detail in ref. 31).

By taking into account group-theoretical conditions for ground and excited states, this approach examines the possibility of spontaneous displacements of an arbitrary atom from the centre of an anion polyhedron. The energy change in the electronic Hamiltonian (H_0) of the high-symmetry parent phase as a result of the small displacements (Q) can be written in the form of a Taylor–Maclaurin series within second-order perturbation theory.^{94,95}

$$H = H^{(0)} + H^{(1)}Q + 1/2H^{(2)}Q^2 + \dots,$$

where

$$H^{(1)} \equiv dH/dQ \text{ and } H^{(2)} \equiv d^2H/dQ^2. \quad (1)$$

In this way, the total energy (E) of a system is calculated in the form:

$$E = E_0 + \langle 0|H^{(1)}|0 \rangle Q + \frac{1}{2} \left[\langle 0|H^{(2)}|0 \rangle - 2 \sum_n \left[\frac{|\langle 0|H^{(1)}|n \rangle|^2}{(E_n - E_0)} \right] \right] Q^2, \quad (2)$$

where E_0 and E_n are the energies of the ground $|0\rangle$ and excited $|n\rangle$ states, respectively. The first-order term $\langle 0|H^{(1)}|0\rangle Q$ is always positive for nondegenerate electronic ground states (the theorem of instability⁹⁶), while for degenerate electronic states it is described according to the first-order Jahn–Teller theorem, which leads only to centrosymmetric distortion (for d orbitals and centrosymmetric parent phase) of the anion polyhedron due to the displacements of the ligand atoms. The second-order term, being the only course of structural instability in nondegenerate system, describes the competition between short-range repulsive forces (term $\langle 0|H^{(2)}|0\rangle$ trends to increase the energy of the system with distortion, always positive) and energy gain due to covalent bond formation (term $-2 \sum_n \left[\frac{|\langle 0|H^{(1)}|n \rangle|^2}{(E_n - E_0)} \right]$ is always negative and favors local off-centric displacements). Therefore, in order to achieve local symmetry breaking *via* the pseudo Jahn–Teller effect, the energy gap $E_n - E_0$ in the denominator should be small and the matrix elements in the numerator should have non-zero values. The last condition is satisfied only if the direct product of the irreducible representation (irrep) for ground (Γ_0) and excited (Γ_n) states spans Q (Q and $H^{(1)}$ are transformed by the same irrep):

$$\Gamma_n \otimes \Gamma_0 \supset Q,$$

which means the symmetry selection rule for the mixing of states in the response of a certain type of distortion (according to the irrep) and *vice versa*.

Following Bersuker,⁹⁷ we consider MO₆⁸⁻ cluster in the parent perovskite structure with a space group $Pm\bar{3}m$ from the point of symmetry-allowed possibility of ferroelectric structural instability (off-centred displacement of the M-atom)

described by irrep $\Gamma_{4-}(t_{1u})$ (a).¹⁰² According to the principal group-theoretical relation between irreps of polar distortion, ground and excited states, we need to analyse pairs Γ_n and Γ_o for every possible valence configuration of the M atom in the SrTiO:M single crystal. For perovskites with a d^0 electronic configuration, the valence band (highest occupied molecular orbital, HOMO) mainly consists of 2p states of oxygen, and the bottom of the conduction band (lowest unoccupied molecular orbital, LUMO) of transition-metal 3d states, which are transformed according to different irreps $\Gamma_{4-}(t_{1u})$ and $\Gamma_{5+}(t_{2g})$, respectively.

Thus, orbital overlap is forbidden by symmetry. However, the displacement of the M cation *via* $\Gamma_{4-}(t_{1u})$ polar distortion leads to lowering the symmetry to $P4mm$ space group and related splitting of the electronic states: $\Gamma_{4-}(t_{1u}) \rightarrow \Gamma_{1+}(a_{1g}) + \Gamma_{5+}(t_{2g})$ and $\Gamma_{5+}(t_{2g}) \rightarrow \Gamma_{3+}(e_g) + \Gamma_{5+}(t_{2g})$. As a result, HOMO and LUMO (2/3) states transform by the same irrep $\Gamma_{5+}(t_{2g})$, lifting the symmetry construction for orbital mixing, which allows activation (but is not a sufficient condition) of the pseudo Jahn–Teller effect. This symmetry-based mechanism of the local distortion is well known for ferroelectric phase transitions in many d^0 perovskites, for example, BaTiO₃, but expanding this approach makes it possible to list other possible electronic configurations of the transition metal for which the manifestation of the effect is not prohibited by symmetry.⁹⁷

For the case of sufficiently large $e_g - t_{2g}$ separation (strong octahedral ligand field), the d_3 , d_4 and d_5 (for both strong and

weak splitting) electronic configurations provide opportunity for the pseudo Jahn–Teller effect and ferroelectric instability, while for d_6 and d_7 states, this option is prohibited by symmetry (for strong octahedral ligand field).⁹⁷ This means that in the case of manganese at the centre of the octahedron, the symmetry allows the pseudo Jahn–Teller effect to manifest, leading to the observable off-centred position for all possible states Mn^{4+} , Mn^{3+} and Mn^{2+} (Fig. 6b). However, our experimental results indicate the absence of a significant amount of compensated oxygen vacancies in the structure of the STO:Mn single crystal, which implies the preferred IV valence for the Mn ions. Arguments in favour of this include the invariance of the parameters of the Axe mode in comparison with pure STO,¹⁰³ the weak high-temperature anomaly of $\tan \delta$ (Fig. 4b), and a decrease in the T_a by ~ 20 K.¹⁰³ Similar mechanisms of ferroelectricity and multiferroicity have been observed in other d^3 perovskites, including CaMnO₃ at negative pressure,¹⁰⁴ solid solutions (Ba,Ca)MnO₃¹⁰⁵ and (Ba,Sr)MnO₃,¹⁰⁶ and the predicted $Amm2$ phase of BaMnO₃.¹⁰¹

In contrast to manganese ions in STO with a more preferred IV valence state without reduction atmosphere,¹⁰⁷ iron ions favour having III or mixed III/IV states,^{59–61} which inevitably means the formation of compensating defects—oxygen vacancies.⁴⁸ While both electronic states d^5 and d^4 allow the pseudo Jahn–Teller effect and atomic off centring, the d^4 electronic configuration is degenerate, which can lead to the oxygen octahedron distortion *via* the first-order Jahn–Teller

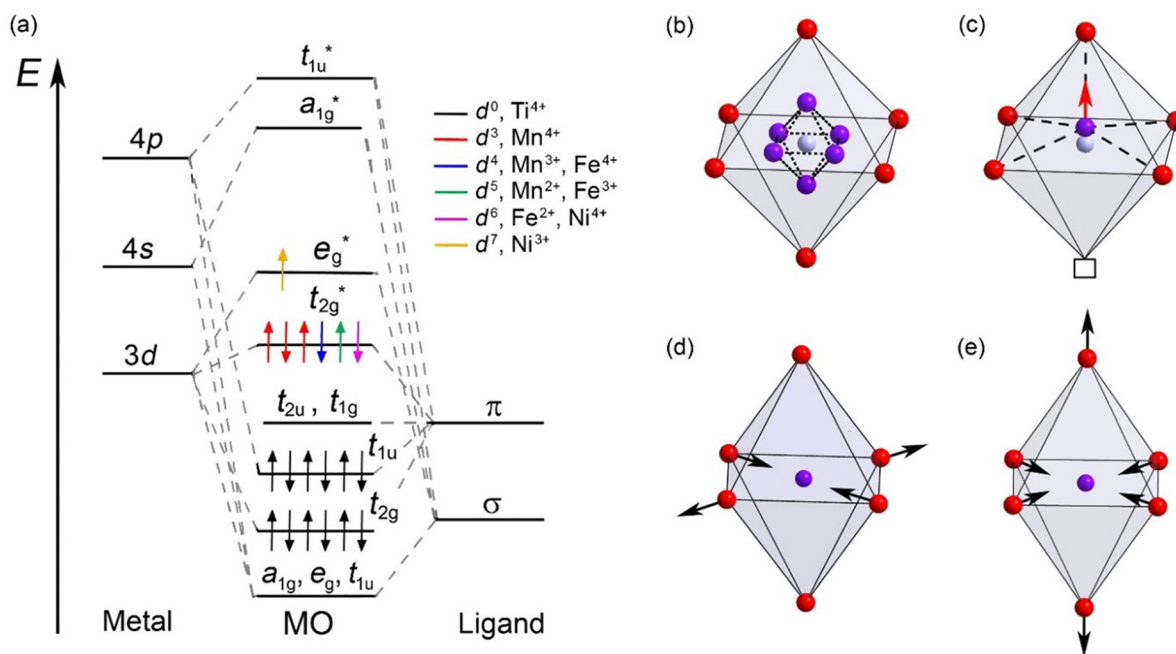


Fig. 6 (a) Energy-level scheme of the molecular orbital (MO) formation in the MO₆ octahedral cluster¹⁰² with the most probable electronic configurations for the B-substituted SrTiO₃:M (Mn, Fe, Ni). Electrons at the lowest energy levels (a_{1g} , e_g , and t_{1u}), as well as electrons at levels originating predominantly from ligands (t_{2u} and t_{1g}), are not shown. (b)–(e) Structural mechanisms of local distortions. (b) Off-centring position of the M-cation (with reduced occupancy 1/6), providing the possibility for atomic hopping. Probable hopping pathways are shown with dotted lines. (c) Vacancy-induced distortion: M-cation (as well as Ti) shifts toward the opposite oxygen. The displacements of oxygen atoms are not shown. (d) and (e) Jahn–Teller type of distortion: Q_2 and Q_3 normal modes. Oxygen atoms are shown in red, M-cations in purple, oxygen vacancy in square, and the central position (empty) in blue.

effect. Note that Jahn–Teller distortion is usually dominant in electronically degenerate systems, and it does not lead to ferroelectric instability in contrast to the pseudo Jahn–Teller effect, which is caused by energy balance. According to our experimental data, there are no additional lines characteristic of Fe^{4+} in the Raman spectra (Fig. 3),^{61,77,80} and the dielectric anomalies associated with oxygen vacancies are the strongest in comparison with other doped crystals (Fig. 4b).

Note that both low- and high-temperature dielectric anomalies are significantly suppressed after high-temperature annealing (Fig. S7, ESI†), which does not affect the dielectric anomaly in Mn-doped single crystals (Fig. S6, ESI†). To reveal the valence state of Fe, we obtained the Mössbauer spectrum of the crystal (Fig. S8 and Table S2, ESI†), the analysis of which unambiguously confirms the +3 state of Fe, which is typical for doped STO single crystals.^{108,109} This indicates the existence of compensated defect complexes, in particular $\text{Fe}^{3+}\text{-VO}$, in the structure of STO:Fe single crystals. In fact, the presence of oxygen vacancies can lead to distortion of the local environment of iron atoms even without a pseudo Jahn–Teller effect (Fig. 6c). For example, according to first-principle calculations, Ti ions are shifted from the V_{O} by 0.11 Å along the (100) direction.⁸⁰ The displacement of iron atoms that we discovered is twice as large, but we cannot establish unambiguously whether this is the effect of only local distortion due to the presence of oxygen vacancies or a combination of several mechanisms (distortion from oxygen vacancies (Fig. 6c) and Fe^{3+} displacement *via* pseudo Jahn–Teller effect (Fig. 6b)). The absence of such dielectric relaxation in STO:Ni (probably Ni^{3+} , see below) favours a complex effect in STO:Fe. More importantly, temperature-activated reorientation of such defect complexes would be expected to have larger activation barriers compared to single atomic hopping, which allows us to explain the significant difference in E_{a} values (Fig. 5) for STO:Fe (120 meV) and STO:Mn (35 meV).

According to our results of single crystal X-ray diffraction, nickel atoms are located in the centre of the oxygen octahedron, which can also be understood in terms of the symmetry-forbidden pseudo Jahn–Teller effect.⁹⁷ In this regard, nickel ions with the most probable valence states (III, IV) for the B-substituted STO^{55,57} appear to be less prone to local off-centring within the oxygen octahedron. Although for non-low-spin configurations this hypothetical possibility remains, for systems with electron degeneracy the first-order perturbation term (the second term in eqn (1)) dominates, leading to Jahn–Teller distortion of the octahedron. This structural distortion is associated only with a certain type of ligand (oxygen atom) displacement (Fig. 6d and e), *i.e.*, the cation remains at the centre of the octahedron. This is why we do not detect signs of Jahn–Teller distortion based on the results of single-crystal X-ray diffraction (that is weakly sensitive to the position of oxygen atoms), although some additional electron density is still observed (Fig. 1e and h). In this case, Raman spectra are more sensitive to local distortions demonstrating peaks at a frequency of 665 cm^{-1} characteristic of STO doped with a Jahn–Teller-active ion Fe^{4+} (Fig. 3).⁶¹ This is also consistent with the

temperature behaviour of the mode parameters (frequency, intensity, and FWHM): when cooled, they behave very similar to B–O bond-stretching modes (Fig. 6d and e) in the known Jahn–Teller-systems.^{72–75,110} The appearance of local Jahn–Teller distortion in the structure of STO:Ni crystals may be a source of Jahn–Teller polarons and the accompanying contribution to conductivity and unusual dielectric behaviour (Fig. 4 and 5).^{111,112} Note that at low impurity concentrations, the influence of the effects of covalence and delocalization of electrons is not so strong, which contributes to the Jahn–Teller effect on isolated nickel centres. In the case of STO with $\text{Fe}^{4+}(x)$, the strongest Jahn–Teller distortion was observed in the regime of low concentration $x = 0.03$, weakening with increasing concentration x .

Thus, based on the fundamental possibility of the local off-centring of impurity ions in the octahedral environment, we were able to identify the main mechanisms for the formation of structural distortions and macroscopic responses. Of course, in real doped STO crystals, valence mixing is common, blurring the signatures of the discussed effects, which may coexist or compete. However, we tried to emphasize the most dominant structural mechanisms based on a set of experimental data and not on the nominal valences and conditional radii of impurity atoms, which is sometimes effective for solid solutions with significant changes in concentrations. Nevertheless, based on our generalized conclusions, such reasoning (strictly speaking, it is of little use at low impurity concentrations) becomes less speculative. For instance, by considering the Shannon ionic radii (Table S3, ESI†)¹¹³ and assessing the space for potential displacements of the impurity ion within the anion octahedron, it can be inferred that the Mn^{4+} ion ($R = 0.53\text{ Å}$ in comparison with $R = 0.605\text{ Å}$ for the ion Ti^{4+}) is likely to undergo a significant off-centred displacement, whereas the space for the Ni^{3+} ($R = 0.56/0.6\text{ Å}$) and Fe^{3+} ($R = 0.55/0.645\text{ Å}$) ions is significantly constrained. In the latter case, a significant difference in the dielectric behaviour for geometrically close substituted cations (Fe^{3+} and Ni^{3+}), which are probably accompanied by the appearance of oxygen vacancies, emphasizes the fundamental role of the electronic structure discussed above.

6. Conclusions

In summary, the results we obtained are of a fundamental nature: for the first time for quantum paraelectrics, the key role of the electronic structure of doping additives in the formation of anomalous structural responses in crystals has been established. We performed a detailed comparative study of the crystal structure, Raman and terahertz-infrared spectra, as well as the low-frequency dielectric properties of SrTiO_3 crystals doped with the transition metals Mn, Ni, and Fe. Our results indicate that the addition of these 3d atoms, which are similar in chemical nature and occupy adjacent positions in the Periodic Table of Elements, has a radically different effect on the properties of quantum paraelectric SrTiO_3 . The origins of the observed phenomena are associated with various

tendencies of impurity atoms toward local off-centring and creating charge-compensating defects, giving rise to a diversity of structural mechanisms of dipole formation. Our comprehensive research reveals that these mechanisms dominate in the form of the pseudo Jahn–Teller effect for Mn-doped SrTiO₃ and the first-order Jahn–Teller effect for Ni-doped crystal, while the Fe-impurity largely contributes to defect-induced distortions. This study provides a thorough insight into the intricate structure–property relationships, induced by the weak transition metal doping in the SrTiO₃ crystals, as well as in other perovskite compounds. Moreover, it advances our understanding of the structural mechanisms of dipole formation in a wide class of crystals with an octahedral framework based on vibronic coupling theory. This means that our findings open up fundamentally new possibilities for the practical solution of a complicated problem: controlling the dielectric responses of quantum paraelectrics by choosing the type of chemical additive.

Author contributions

Mikhail V. Talanov: formal analysis, conceptualization, writing (original draft), visualisation. Adam I. Stash and Sergey A. Ivanov: single crystal X-ray diffraction, writing (review & editing). Elena S. Zhukova: THz-IR spectroscopy, funding acquisition, writing (review & editing). Boris P. Gorshunov: supervision, conceptualization, writing (review & editing). Boris M. Nekrasov: THz-IR spectroscopy, visualisation, writing (review & editing). Alexander V. Melentev, Ilya A. Zavidovskiy, Mikhail K. Tatmyshevskiy: Raman spectroscopy. Vladislav I. Kozlov and Alexander A. Bush: single crystal growth, writing (review & editing). Valery M. Cherepanov: Mössbauer spectroscopy. Sergey Yu. Gavrilkin and Aleksey Yu. Tsvetkov: magnetic measurements. Maxim Savinov and Valeriy M. Talanov: discussion, writing (review & editing).

Conflicts of interest

There are no conflicts to declare.

Acknowledgements

We acknowledge fruitful discussions with Prof. M. Dressel and Prof. J. Petzelt. We thank O. Glaz for the SEM-EDS analysis. The study was funded by the Russian Science Foundation via Research Projects 21-12-00358 (THz, IR experiments, data analysis), 22-13-00122 (single crystal X-ray diffraction) and 22-72-10022 (theoretical interpretation), and by the Ministry of Science and Higher Education of the Russian Federation via Research Project No. 075-15-2022-1150 (Raman).

Notes and references

1 S. M. Sze, Y. Li and K. K. Ng, *Physics of Semiconductor Devices*, Wiley, 2021.

- H. Liu, Y. Liu and D. Zhu, *J. Mater. Chem.*, 2011, **21**, 3335–3345.
- J. T. E. Quinn, J. Zhu, X. Li, J. Wang and Y. Li, *J. Mater. Chem. C*, 2017, **5**, 8654–8681.
- G. Xu, S. Zeng, B. Zhang, M. T. Swihart, K.-T. Yong and P. N. Prasad, *Chem. Rev.*, 2016, **116**, 12234–12327.
- Y. Wang, J. Su, Z. Lin, J. Zhang, J. Chang and Y. Hao, *J. Mater. Chem. C*, 2022, **10**, 13395–13436.
- A. D. Scaccabarozzi, A. Basu, F. Anié, J. Liu, O. Zapata-Arteaga, R. Warren, Y. Firdaus, M. I. Nugraha, Y. Lin and M. Campoy-Quiles, *Chem. Rev.*, 2021, **122**, 4420–4492.
- D. Li, D. Wang, X. Zhang and L.-D. Zhao, *J. Mater. Chem. C*, 2022, **10**, 13851–13859.
- B. Luo, F. Li, K. Xu, Y. Guo, Y. Liu, Z. Xia and J. Z. Zhang, *J. Mater. Chem. C*, 2019, **7**, 2781–2808.
- D. Jana, C.-L. Sun, L.-C. Chen and K.-H. Chen, *Prog. Mater. Sci.*, 2013, **58**, 565–635.
- Y. Wang, W. Jie, C. Yang, X. Wei and J. Hao, *Adv. Funct. Mater.*, 2019, **29**, 1808118.
- W. Hu, Y. Liu, R. L. Withers, T. J. Frankcombe, L. Norén, A. Snashall, M. Kitchin, P. Smith, B. Gong, H. Chen, J. Schiemer, F. Brink and J. Wong-Leung, *Nat. Mater.*, 2013, **12**, 821–826.
- N. T. Taylor, F. H. Davies, S. G. Davies, C. J. Price and S. P. Hepplestone, *Adv. Mater.*, 2019, **31**, 1904746.
- P. Leret, J. F. Fernandez, J. de Frutos and D. Fernández-Hevia, *J. Eur. Ceram. Soc.*, 2007, **27**, 3901–3905.
- G. Chiodelli, V. Massarotti, D. Capsoni, M. Bini, C. B. Azzoni, M. C. Mozzati and P. Lupotto, *Solid State Commun.*, 2004, **132**, 241–246.
- H. Kishi, Y. Mizuno and H. Chazono, *Jpn. J. Appl. Phys.*, 2003, **42**, 1.
- A. R. West, T. B. Adams, F. D. Morrison and D. C. Sinclair, *J. Eur. Ceram. Soc.*, 2004, **24**, 1439–1448.
- S. Guillemet, Z. Valdez Nava, C. Tenailleau, T. Lebey, B. Durand and J.-Y. Chane-Ching, *Adv. Mater.*, 2008, **20**, 551–555.
- V. Fallah, B. Langelier, N. Ofori-Opoku, B. Raeisinia, N. Provatas and S. Esmaeili, *Acta Mater.*, 2016, **103**, 290–300.
- J. Wu, C.-W. Nan, Y. Lin and Y. Deng, *Phys. Rev. Lett.*, 2002, **89**, 217601.
- D. Phelan, C. Stock, J. A. Rodriguez-Rivera, S. Chi, J. Leão, X. Long, Y. Xie, A. A. Bokov, Z.-G. Ye, P. Ganesh and P. M. Gehring, *Proc. Natl. Acad. Sci.*, 2014, **111**, 1754–1759.
- V. Westphal, W. Kleemann and M. D. Glinchuk, *Phys. Rev. Lett.*, 1992, **68**, 847–850.
- J. R. Arce-Gamboa and G. G. Guzmán-Verri, *npj Quantum Materials*, 2017, **2**, 28.
- R. Pirc and R. Blinc, *Phys. Rev. B: Condens. Matter Mater. Phys.*, 1999, **60**, 13470–13478.
- M. V. Talanov, A. A. Bokov and M. A. Marakhovskiy, *Acta Mater.*, 2020, **193**, 40–50.
- B. E. Vugmeister and M. D. Glinchuk, *Rev. Mod. Phys.*, 1990, **62**, 993–1026.
- F. Li, M. J. Cabral, B. Xu, Z. Cheng, E. C. Dickey, J. M. LeBeau, J. Wang, J. Luo, S. Taylor, W. Hackenberger,

- L. Bellaiche, Z. Xu, L.-Q. Chen, T. R. ShROUT and S. Zhang, *Science*, 2019, **364**, 264–268.
- 27 F. Li, D. Lin, Z. Chen, Z. Cheng, J. Wang, C. Li, Z. Xu, Q. Huang, X. Liao, L.-Q. Chen, T. R. ShROUT and S. Zhang, *Nat. Mater.*, 2018, **17**, 349–354.
- 28 B. Jaffe, W. Cook and H. Jaffe, *Piezoelectric Ceramics*, Academic Press, London, 1971.
- 29 Y. Feng, J. Wu, Q. Chi, W. Li, Y. Yu and W. Fei, *Chem. Rev.*, 2020, **120**, 1710–1787.
- 30 D. Damjanovic, *Rep. Prog. Phys.*, 1998, **61**, 1267.
- 31 R. A. Maier, E. Cockayne, M. Donohue, G. Cibin and I. Levin, *Chem. Mater.*, 2020, **32**, 4651–4662.
- 32 S. E. Rowley, L. J. Spalek, R. P. Smith, M. P. M. Dean, M. Itoh, J. F. Scott, G. G. Lonzarich and S. S. Saxena, *Nat. Phys.*, 2014, **10**, 367–372.
- 33 P. Chandra, G. G. Lonzarich, S. E. Rowley and J. F. Scott, *Rep. Prog. Phys.*, 2017, **80**, 112502.
- 34 J. H. Haeni, P. Irvin, W. Chang, R. Uecker, P. Reiche, Y. L. Li, S. Choudhury, W. Tian, M. E. Hawley, B. Craigo, A. K. Tagantsev, X. Q. Pan, S. K. Streiffer, L. Q. Chen, S. W. Kirchoefer, J. Levy and D. G. Schlom, *Nature*, 2004, **430**, 758–761.
- 35 H. Uwe and T. Sakudo, *Phys. Rev. B: Solid State*, 1976, **13**, 271–286.
- 36 P. A. Fleury and J. M. Worlock, *Phys. Rev.*, 1968, **174**, 613–623.
- 37 X. Li, T. Qiu, J. Zhang, E. Baldini, J. Lu, A. M. Rappe and K. A. Nelson, *Science*, 2019, **364**, 1079–1082.
- 38 J. G. Bednorz and K. A. Müller, *Phys. Rev. Lett.*, 1984, **52**, 2289–2292.
- 39 V. B. Shirokov, V. I. Torgashev, A. A. Bakirov and V. V. Lemanov, *Phys. Rev. B: Condens. Matter Mater. Phys.*, 2006, **73**, 104116.
- 40 U. Bianchi, J. Dec, W. Kleemann and J. G. Bednorz, *Phys. Rev. B: Condens. Matter Mater. Phys.*, 1995, **51**, 8737–8746.
- 41 V. Lemanov, *Ferroelectrics*, 1999, **226**, 133–146.
- 42 M. Itoh, R. Wang, Y. Inaguma, T. Yamaguchi, Y. J. Shan and T. Nakamura, *Phys. Rev. Lett.*, 1999, **82**, 3540–3543.
- 43 K. Klyukin and V. Alexandrov, *Phys. Rev. B: Condens. Matter Mater. Phys.*, 2017, **95**, 035301.
- 44 A. Tkach, P. M. Vilarinho, A. L. Kholkin, A. Pashkin, S. Veljko and J. Petzelt, *Phys. Rev. B: Condens. Matter Mater. Phys.*, 2006, **73**, 104113.
- 45 V. V. Shvartsman, S. Bedanta, P. Borisov, W. Kleemann, A. Tkach and P. M. Vilarinho, *Phys. Rev. Lett.*, 2008, **101**, 165704.
- 46 J. F. Schooley, W. R. Hosler and M. L. Cohen, *Phys. Rev. Lett.*, 1964, **12**, 474–475.
- 47 A. Narayan, A. Cano, A. V. Balatsky and N. A. Spaldin, *Nat. Mater.*, 2019, **18**, 223–228.
- 48 R. Merkle and J. Maier, *Angew. Chem., Int. Ed.*, 2008, **47**, 3874–3894.
- 49 S. Steinsvik, R. Bugge, J. O. N. GjØNnes, J. TaftØ and T. Norby, *J. Phys. Chem. Solids*, 1997, **58**, 969–976.
- 50 X. Yuan, L. Meng, C. Zheng and H. Zhao, *ACS Appl. Mater. Interfaces*, 2021, **13**, 52571–52587.
- 51 Y. Yoshiyama, S. Hosokawa, H. Asakura, K. Teramura and T. Tanaka, *J. Phys. Chem. C*, 2022, **126**, 4415–4422.
- 52 F. Zhong, L. Wang, H. Fang, Y. Luo, C. Chen, L. Lin, K. Chen and L. Jiang, *Chem. Eng. J.*, 2023, **471**, 144650.
- 53 C. Garg, J. Kumar and S. Nair, *Phys. Rev. Mater.*, 2018, **2**, 094409.
- 54 M. V. Talanov, A. I. Stash, S. A. Ivanov, E. S. Zhukova, B. P. Gorshunov, B. M. Nekrasov, V. S. Stolyarov, V. I. Kozlov, M. Savinov and A. A. Bush, *J. Phys. Chem. Lett.*, 2022, **13**, 11720–11728.
- 55 I. A. Sluchinskaya, A. I. Lebedev and A. Erko, *Phys. Solid State*, 2014, **56**, 449–455.
- 56 A. M. Beale, M. Paul, G. Sankar, R. J. Oldman, C. R. A. Catlow, S. French and M. Fowles, *J. Mater. Chem.*, 2009, **19**, 4391–4400.
- 57 K. A. Müller, W. Berlinger and R. S. Rubins, *Phys. Rev.*, 1969, **186**, 361–371.
- 58 S.-Y. Wu, J.-Z. Lin, Q. Fu and H.-M. Zhang, *Phys. Scr.*, 2007, **75**, 147.
- 59 L. F. D. Silva, J.-C. M'Peko, J. Andrés, A. Beltrán, L. Gracia, M. I. B. Bernardi, A. Mesquita, E. Antonelli, M. L. Moreira and V. R. Mastelaro, *J. Phys. Chem. C*, 2014, **218**, 4930–4940.
- 60 A. Rothschild, W. Menesklou, H. L. Tuller and E. Ivers-Tiffée, *Chem. Mater.*, 2006, **18**, 3651–3659.
- 61 M. Vračar, A. Kuzmin, R. Merkle, J. Purans, E. A. Kotomin, J. Maier and O. Mathon, *Phys. Rev. B: Condens. Matter Mater. Phys.*, 2007, **76**, 174107.
- 62 J. Petzelt, T. Ostapchuk, I. Gregora, I. Rychetský, S. Hoffmann-Eifert, A. V. Pronin, Y. Yuzyuk, B. P. Gorshunov, S. Kamba, V. Bovtun, J. Pokorný, M. Savinov, V. Porokhonsky, D. Rafaja, P. Vaněk, A. Almeida, M. R. Chaves, A. A. Volkov, M. Dressel and R. Waser, *Phys. Rev. B: Condens. Matter Mater. Phys.*, 2001, **64**, 184111.
- 63 J. C. Galzerani and R. S. Katiyar, *Solid State Commun.*, 1982, **41**, 515–519.
- 64 H. Vogt and G. Rossbroich, *Phys. Rev. B: Condens. Matter Mater. Phys.*, 1981, **24**, 3086–3091.
- 65 G. Rupprecht and R. O. Bell, *Phys. Rev.*, 1962, **125**, 1915–1920.
- 66 S. Kamba, *APL Mater.*, 2021, **9**, 020704.
- 67 J. Petzelt, G. V. Kozlov and A. A. Volkov, *Ferroelectrics*, 1987, **73**, 101–123.
- 68 S. Kamba, E. Buixaderas, T. Ostapchuk and J. Petzelt, *Ferroelectrics*, 2002, **268**, 163–168.
- 69 A. Tkach, P. M. Vilarinho, D. Nuzhnyy and J. Petzelt, *Acta Mater.*, 2010, **58**, 577–582.
- 70 W. G. Nilsen and J. G. Skinner, *J. Chem. Phys.*, 2003, **48**, 2240–2248.
- 71 M. N. Iliev, M. V. Abrashev, J. Laverdière, S. Jandl, M. M. Gospodinov, Y. Q. Wang and Y. Y. Sun, *Phys. Rev. B: Condens. Matter Mater. Phys.*, 2006, **73**, 064302.
- 72 M. N. Iliev and M. V. Abrashev, *J. Raman Spectrosc.*, 2001, **32**, 805–811.
- 73 M. V. Abrashev, J. Bäckström, L. Börjesson, V. N. Popov, R. A. Chakalov, N. Kolev, R. L. Meng and M. N. Iliev, *Phys. Rev. B: Condens. Matter Mater. Phys.*, 2002, **65**, 184301.

- 74 R. Vilarinho, D. J. Passos, E. C. Queirós, P. B. Tavares, A. Almeida, M. C. Weber, M. Guennou, J. Kreisel and J. A. Moreira, *Phys. Rev. B: Condens. Matter Mater. Phys.*, 2018, **97**, 144110.
- 75 N. Orlovskaya, D. Steinmetz, S. Yarmolenko, D. Pai, J. Sankar and J. Goodenough, *Phys. Rev. B: Condens. Matter Mater. Phys.*, 2005, **72**, 014122.
- 76 N. Kolev, C. L. Chen, M. Gospodinov, R. P. Bontchev, V. N. Popov, A. P. Litvinchuk, M. V. Abrashev, V. G. Hadjiev and M. N. Iliev, *Phys. Rev. B: Condens. Matter Mater. Phys.*, 2002, **66**, 014101.
- 77 V. E. Alexandrov, J. Maier and R. A. Evarestov, *Phys. Rev. B: Condens. Matter Mater. Phys.*, 2008, **77**, 075111.
- 78 A. Tkach, P. M. Vilarinho, A. L. Kholkin, A. Pashkin, P. Samoukhina, J. Pokorný, S. Veljko and J. Petzelt, *J. Appl. Phys.*, 2005, **97**, 044104.
- 79 H. Zheng, I. M. Reaney, G. D. C. C. de Györgyfalva, R. Ubic, J. Yarwood, M. P. Seabra and V. M. Ferreira, *J. Mater. Res.*, 2011, **19**, 488–495.
- 80 E. Blokhin, E. Kotomin, A. Kuzmin, J. Purans, R. Evarestov and J. Maier, *Appl. Phys. Lett.*, 2013, **102**, 112913.
- 81 C. Ang, J. F. Scott, Z. Yu, H. Ledbetter and J. L. Baptista, *Phys. Rev. B: Condens. Matter Mater. Phys.*, 1999, **59**, 6661–6664.
- 82 K. A. Müller and H. Burkard, *Phys. Rev. B: Condens. Matter Mater. Phys.*, 1979, **19**, 3593–3602.
- 83 O. E. Kvyatkovskii, *Phys. Solid State*, 2001, **43**, 1401–1419.
- 84 L. Pálová, P. Chandra and P. Coleman, *Phys. Rev. B: Condens. Matter Mater. Phys.*, 2009, **79**, 075101.
- 85 S. A. Hayward, F. D. Morrison and J. F. Scott, *J. Phys.: Condens. Matter*, 2005, **17**, 7009.
- 86 J. H. Barrett, *Phys. Rev.*, 1952, **86**, 118–120.
- 87 M. Savinov, V. A. Trepakov, P. P. Syrnikov, V. Železný, J. Pokorný, A. Dejneka, L. Jastrabík and P. Galinetto, *J. Phys.: Condens. Matter*, 2008, **20**, 095221.
- 88 A. S. Nowick, S. Q. Fu, W. K. Lee, B. S. Lim and T. Scherban, *Mater. Sci. Eng., B*, 1994, **23**, 19–24.
- 89 I. Bykov, I. Geifman, M. Glinchuk and B. Krulikovskii, *Trans. Sov. Phys. Solid State*, 1980, **22**, 1248.
- 90 E. Siegel and K. A. Müller, *Phys. Rev. B: Condens. Matter Mater. Phys.*, 1979, **19**, 109–120.
- 91 R. Viana, P. Lunkenheimer, J. Hemberger, R. Böhmer and A. Loidl, *Phys. Rev. B: Condens. Matter Mater. Phys.*, 1994, **50**, 601–604.
- 92 A. K. Tagantsev, E. Courtens and L. Arzel, *Phys. Rev. B: Condens. Matter Mater. Phys.*, 2001, **64**, 224107.
- 93 O. Bidault, M. Maglione, M. Actis, M. Kchikech and B. Salce, *Phys. Rev. B: Condens. Matter Mater. Phys.*, 1995, **52**, 4191–4197.
- 94 J. K. Burdett, *Inorg. Chem.*, 1981, **20**, 1959–1962.
- 95 R. G. Pearson, *J. Mol. Struct. THEOCHEM*, 1983, **103**, 25–34.
- 96 I. B. Bersuker, *Chem. Rev.*, 2021, **121**, 1463–1512.
- 97 I. B. Bersuker, *Phys. Rev. Lett.*, 2012, **108**, 137202.
- 98 P. García-Fernández, J. A. Aramburu, M. Moreno, M. Zlatař and M. Gruden-Pavlović, *J. Chem. Theory Comput.*, 2014, **10**, 1824–1833.
- 99 T. Azumi and K. Matsuzaki, *Photochem. Photobiol.*, 1977, **25**, 315–326.
- 100 S. Yoshida, H. Akamatsu and K. Hayashi, *Phys. Rev. Lett.*, 2021, **127**, 215701.
- 101 J. M. Rondinelli, A. S. Eidelson and N. A. Spaldin, *Phys. Rev. B: Condens. Matter Mater. Phys.*, 2009, **79**, 205119.
- 102 H. B. Gray, *J. Chem. Educ.*, 1964, **41**, 2.
- 103 M. V. Talanov, E. S. Zhukova, B. M. Nekrasov, M. Savinov, V. I. Kozlov, B. P. Gorshunov and A. A. Bush, *JETP Lett.*, 2023, **118**, 684.
- 104 P. Barone, S. Kanungo, S. Picozzi and T. Saha-Dasgupta, *Phys. Rev. B: Condens. Matter Mater. Phys.*, 2011, **84**, 134101.
- 105 S. Bhattacharjee, E. Bousquet and P. Ghosez, *Phys. Rev. Lett.*, 2009, **102**, 117602.
- 106 H. Sakai, J. Fujioka, T. Fukuda, D. Okuyama, D. Hashizume, F. Kagawa, H. Nakao, Y. Murakami, T. Arima, A. Q. R. Baron, Y. Taguchi and Y. Tokura, *Phys. Rev. Lett.*, 2011, **107**, 137601.
- 107 A. Tkach, P. M. Vilarinho and A. L. Kholkin, *Acta Mater.*, 2006, **54**, 5385–5391.
- 108 V. Bhide and H. Bhasin, *Phys. Rev.*, 1968, **172**, 290–294.
- 109 M. Multani, *Mat. Res. Bull.*, 1984, **19**, 25–34.
- 110 L. Martín-Carrón and A. de Andrés, *Eur. Phys. J. B*, 2001, **22**, 11–16.
- 111 K. A. Miller, *J. Supercond.*, 1999, **12**, 3–7.
- 112 M. Medarde, P. Lacorre, K. Conder, F. Fauth and A. Furrer, *Phys. Rev. Lett.*, 1998, **80**, 2397–2400.
- 113 R. D. Shannon, *Acta Crystallogr., Sect. A: Cryst. Phys., Diffr., Theor. Gen. Crystallogr.*, 1976, **32**, 751–767.